

Oxidation Behavior of Binary Aluminium-Rich Fe–Al Alloys with a Fine-Scaled, Lamellar Microstructure

A. Scherf · D. Janda · M. Baghaie Yazdi · X. Li ·
F. Stein · M. Heilmaier

Received: 9 December 2014 / Revised: 27 January 2015 / Published online: 10 February 2015
© Springer Science+Business Media New York 2015

Abstract The oxidation behavior of binary Fe–Al alloys with an aluminum content between 58 and 64 at.% was studied by isothermal and cyclic oxidation experiments in a temperature range of 900–1000 °C. The parabolic rate constants were determined to be comparable to those of B2-ordered Fe–48Al. All investigated alloys exhibited a fine-scaled, lamellar microstructure (<300 nm lamellar spacing), which was a result of the eutectoid decomposition of the high-temperature phase Fe₅Al₈ into FeAl and FeAl₂. None of these two phases showed a preferential oxidation. At 900 °C θ -Al₂O₃ formed, whereas at 1000 °C a transformation of the initially formed θ -Al₂O₃ to the slower growing and passivating α -Al₂O₃ was confirmed by grazing incidence X-ray diffraction measurements.

Keywords FeAl · FeAl₂ · Oxidation · Microstructure

Introduction

The oxidation behavior of iron aluminides with an Al content of up to 50 at.% has been fairly thoroughly investigated in literature [1–5]. In these publications it has been shown that depending on aluminum content and temperature different

A. Scherf (✉) · D. Janda · M. Heilmaier
Institute for Applied Materials, Karlsruhe Institute of Technology, Karlsruhe, Germany
e-mail: anke.scherf@kit.edu

M. Baghaie Yazdi
Institute of Material Science, Technische Universität Darmstadt, Darmstadt, Germany

X. Li · F. Stein
Structure and Nano-/Micromechanics of Materials, Max-Planck-Institut für Eisenforschung,
Düsseldorf, Germany

modifications of alumina are formed. For alloys with less than 15 at.% Al oxidized at 800 °C, iron oxide nodules occur [6]. However, with increasing temperature less aluminum is necessary to generate a dense Al_2O_3 oxide scale. Hence, at 1000 °C, 9 at.% Al is sufficient to obtain a thin, dense alumina scale [5], whereas at 1100 °C only 5 at.% Al is needed [7]. However, in both cases iron oxide is formed underneath the alumina scale [5, 7]. In order to suppress the iron oxide formation completely at 900 °C more than 20 at.% Al are necessary [8]. Since a pure alumina scale is more protective, which expresses itself in a slower oxidation rate [9], it is desirable to prevent the formation of iron oxides completely. Especially the stable $\alpha\text{-Al}_2\text{O}_3$ modification is known for its excellent passivating properties [10]. Besides $\alpha\text{-Al}_2\text{O}_3$, the thermodynamic metastable and less protective modifications $\gamma\text{-Al}_2\text{O}_3$ and $\theta\text{-Al}_2\text{O}_3$ have been observed on Fe–Al alloys [2, 5, 11]. It has been reported that in the initial state of oxidation $\gamma\text{-Al}_2\text{O}_3$ or $\theta\text{-Al}_2\text{O}_3$ is formed, which is then transformed into the stable $\alpha\text{-Al}_2\text{O}_3$ modification upon further timely progress [9]. Rommerskirchen et al. found that for B2-ordered alloys with aluminum contents of 40–48 at.% this transition occurs in a temperature range between 900 and 1000 °C [5]. Thereby, also a change in the morphology of the oxide scale occurs, which was described by Smialek et al. [12]. They associated the fast growing whisker like structure at 900 °C with $\theta\text{-Al}_2\text{O}_3$. At 1000 °C they found that this whisker morphology became coarse and concave cells of $\alpha\text{-Al}_2\text{O}_3$ appeared.

For aluminum contents beyond the B2 FeAl single phase field, in the two-phase region FeAl (cP2 crystal structure) and FeAl_2 (aP19) between 55 and 65 at.% Al, oxidation kinetics have not yet been studied thoroughly. As shown in the phase diagram, Fig. 1, alloys with about 60.5 at.% Al pass through a eutectoid reaction. Although the temperature at the eutectoid decomposition at 1095 °C is rather high, the resulting lamellar microstructure is on a very fine scale involving a high interface density. It is, thus, the aim of the present study to compare the oxidation behavior of two-phase Fe–Al alloys in the compositional range between 58 and

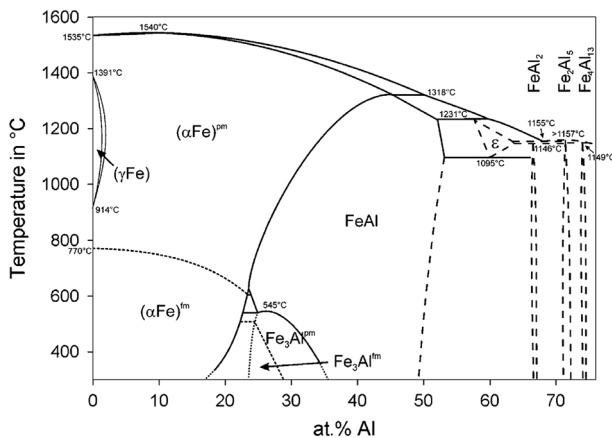


Fig. 1 Phase diagram of the Fe–Al system [15]

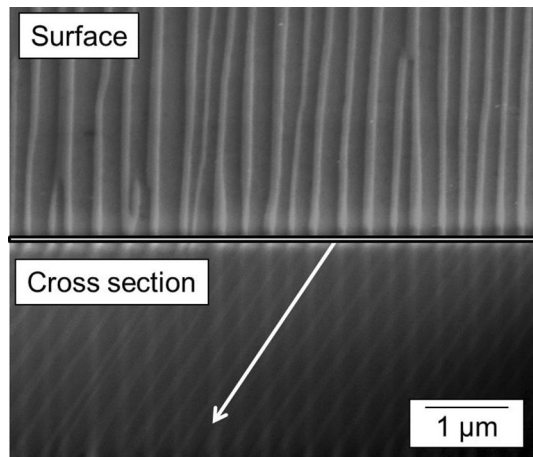
64 at.% Al with those of single phase B2-ordered FeAl. Specifically, it will be clarified if the oxidation mechanisms known from the latter also hold true for these two-phase alloys. Secondly, due to its two-phase microstructure, the potential occurrence of selective oxidation in these alloys will be addressed. Finally, we examine the possibility of internal oxidation. This may likely occur because of the high interface density which promotes fast oxygen inward diffusion through the phase boundaries and has been observed several times already for FeAl alloys [13, 14].

Experimental Procedures

The investigated alloys were produced by arc melting and subsequent casting into a copper mold. The nominal compositions were an Al-lean Fe–58Al, eutectoid Fe–61Al and Al-rich Fe–64Al alloy. Chemical compositions of the major alloying elements were verified by wet chemical analysis and are given in at.%. In addition, the content of the impurity element S was determined by infrared absorption spectroscopy (Leco CS-444).

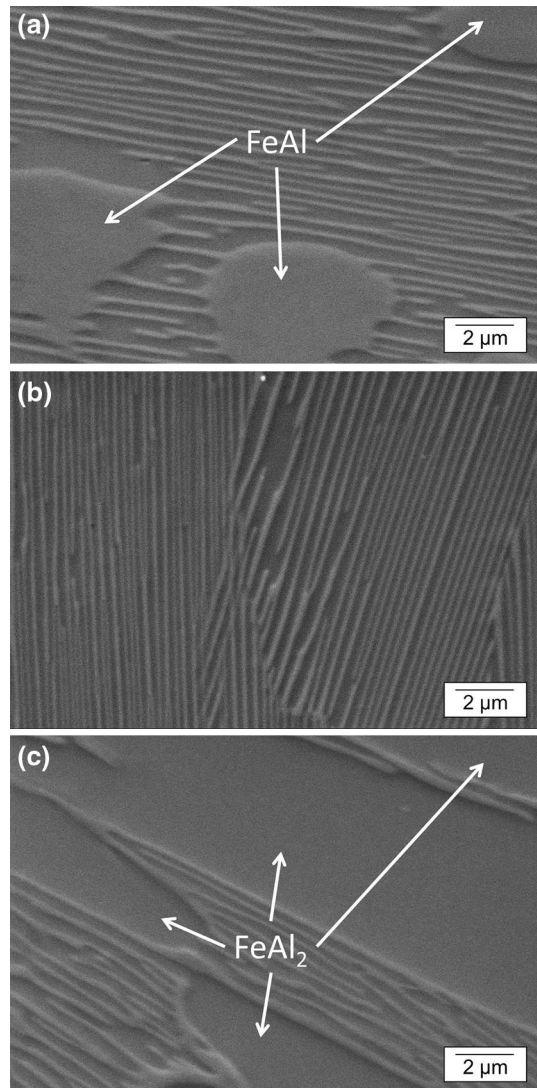
To determine the “true” lamellar spacing of the as-cast state, a combination of scanning electron microscope (SEM) and focused ion beam (FIB) system (Strata 400 S, FEI) was used. The lamellae were first oriented vertically on the screen; then an area of $10\ \mu\text{m}^2$ was milled to a depth of $3\ \mu\text{m}$. An edge with an angle of 90° between surface and cross section resulted. The tilting of the lamellae can then be visualized and measured on the cross section of the prepared sample (see Fig. 2). Note that the formation of striations on the cross section is caused by the curtaining effect during preparation. With the knowledge of how the lamellae were tilted during operation it is possible to determine the true lamellar spacing.

Fig. 2 SEM-SE micrograph of the sample surface with vertically orientated lamellae in the *upper part* of the micrograph and a milled cross-sectional area which (*lower part*) is perpendicular to the sample surface showing the arrangement of the lamellae in a third dimension (*white arrow*)



To determine the oxidation behavior, disks with a diameter of 12 mm and a height of 2 mm were cut out of the cast rods by water-cooled diamond wire saw cutter. All sides of the disks were polished up to a particle size of 10 μm (FEPA 2400-grit) finish. The surface area was imaged by light microscopy and then quantified using the computer program *analySis*. After oxidation, the microstructure and surface morphology of the grown oxides were analyzed by optical microscopy and scanning electron microscopy (LEO EVO50, Zeiss) equipped with an energy dispersive X-ray spectrometer, EDX. The crystal structures of the grown oxides were investigated using a rotating anode X-ray diffractometer (Rigaku SmartLab) in

Fig. 3 SEM-SE micrographs of the microstructure of the as-cast state of, **a** Fe-58Al: lamellar microstructure with FeAl particles, **b** Fe-61Al: lamellar microstructure **c** Fe-64Al: lamellar microstructure and FeAl₂ particles



Bragg–Brentano (XRD) and grazing incidence geometry (GIXRD). The GIXRD scan was measured with an incidence angle of 0.5° . Subsequently, the oxidized samples were coated wet-chemically with nickel to protect the oxide scale during further preparation for cross-sectional investigations.

Continuous isothermal oxidation behavior was studied by thermogravimetry experiments (STA449 F1 Jupiter, Netzsch) in synthetic air (80 % O_2 , 20 % N_2) at 900 and 1000 °C with a flow rate of 30 ml/min. For further comparison, cyclic oxidation experiments were carried out at the same temperatures of 900 and 1000 °C in ambient air up to 550 h. Here, mass change was measured in time-intervals using a microbalance (USP 34 C41, Sartorius). Prior to weighing, the samples were removed from the furnace and air-cooled to room temperature.

Results and Discussion

Microstructure

All investigated alloys show the characteristic lamellar eutectoid microstructure (see Fig. 3a–c). Residual amounts of the high-temperature phase are not present at room temperature, since it is not possible to maintain the high-temperature ϵ -phase at room temperature even by quenching [16]. A lamellar spacing of 263 ± 32 nm in the as-cast state was measured via SEM (SE mode) in 10 different areas. Since all alloys were produced in the same way, the cooling rate was assumed to be similar. Therefore, it is plausible that the lamellar spacing of the eutectoid was nearly equal for all alloys. Within statistical spread, no noticeable gradient in lamella spacing was found in the cast rods.

In principle, the microstructure of the alloys within the investigated compositional range may consist of FeAl or FeAl₂ particles and eutectoid [17]. As expected, the microstructure of the alloy with 58 at.% Al exhibits mainly a fine lamellar microstructure with minor amounts of FeAl particles (see Fig. 3a), whereas FeAl₂ particles are present in the Al-rich alloy Fe–64Al (see Fig. 3c). The alloy Fe–61Al is expected to represent the stoichiometric eutectoid composition, but besides the lamellar eutectoid microstructure (see Fig. 3b) up to 5 vol% of FeAl₂ precipitates (not shown here) are present which indicate a slight deviation from eutectoid composition. For the sake of simplicity this alloy will still be called “eutectoid” in the following.

The determined chemical compositions are listed in Table 1. The measured impurity contents of $S \leq 5$, $C \leq 6$, $N \leq 6$, and $O \leq 40$ wppm (for Fe–58Al and Fe–61Al) and $O \leq 220$ wppm (for Fe–64Al) are on a low level.

Table 1 Chemical composition in at.%

Alloy	Fe	Al
Fe–58Al	bal.	58.4 ± 0.1
Fe–61Al	bal.	60.5 ± 0.1
Fe–64Al	bal.	63.5 ± 0.1

Isothermal Oxidation

The recorded mass gains normalized with the sample surface area are plotted vs. time exemplarily for Fe–61Al at 900 and 1000 °C in Fig. 4a. Generally, all mass gains observed are on a very low level indicating good protection of the bulk material by the growing oxide scale. The mass gain at 900 °C follows a square-root function with a total mass gain of 0.32 mg/cm² after 99 h.

Hence, it is assumed that the oxidation is rate controlled by diffusional processes through a dense and adherent oxide scale and the parabolic rate law is applicable:

$$\left(\frac{\Delta m}{A}\right)^2 = k_p \cdot t \quad (1)$$

The parabolic rate constant k_p was determined by the slope of a plot of squared normalized mass gain vs. time.

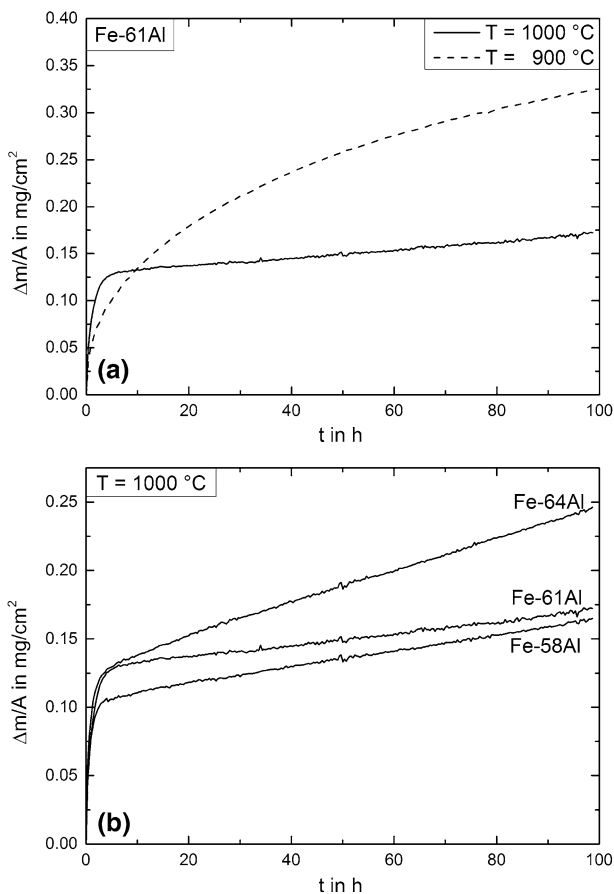


Fig. 4 Mass gain vs. time plot at isothermal conditions: **a** Fe–61Al at 900 and 1000 °C, **b** all investigated alloys at 1000 °C

In comparison, the eutectoid sample oxidized at 1000 °C exhibits a considerable mass gain in the first 2–4 h with a higher overall mass gain than at 900 °C during the same time. Thereafter, the mass gain slows down significantly being even lower than the one observed at 900 °C. This leads to a cross-over of both mass gain curves after 10 h. Consequently, the mass gain curve at 1000 °C can be separated into two regions, indicating a change in the oxidation behavior. To proof if also a change in oxidation kinetics takes place after 2–4 h in the case of the two other alloys, Fe–58Al and Fe–64Al were also tested under isothermal condition at 1000 °C. As shown in Fig. 4b all investigated alloys exhibit the same trend, i.e. a bend in the oxidation curve after 2–4 h. Obviously, the transition time seems to be independent of the volume fraction of the phases present in the bulk material.

If a change in oxidation kinetics occurs like it was observed at 1000 °C two different oxidation rates ($k_{p,I}$ and $k_{p,II}$) may be determined. According to Pieraggi [18] and Smialek [19] two cases may be distinguished: (a) if an initially faster growing scale is not rate controlling oxidation, the $k_{p,II}$ has to be determined by the slope of $(\Delta m - \Delta m_i)^2$ vs. $(t - t_i)$; (b) if the initially formed oxide does contribute to the rate controlling formation of oxide scale, it is reasonable to determine $k_{p,II}$ by the slope of $(\Delta m^2 - \Delta m_i^2)$ vs. $(t - t_i)$ plot. In the following it will be shown that the latter case is more suitable for the upcoming results. Two different slopes are observed in the squared mass gain vs. time plot, which each can be approximated in a linear manner (Fig. 5). The resulting parabolic rate constants k_p for all alloys are listed in Table 2.

The $k_{p,I}$ values (first part of the oxidation curve) for all investigated alloys are with $1\text{--}2 \times 10^{-12} \text{ g}^2 \text{ cm}^{-4} \text{ s}^{-1}$ on the same level. The determined $k_{p,II}$ values (second part of the curve) are all considerably lower, at least by one order of magnitude. In the following, an attempt is made to shed light on these peculiarities of oxidation by microstructural analysis of the growing oxide scale.

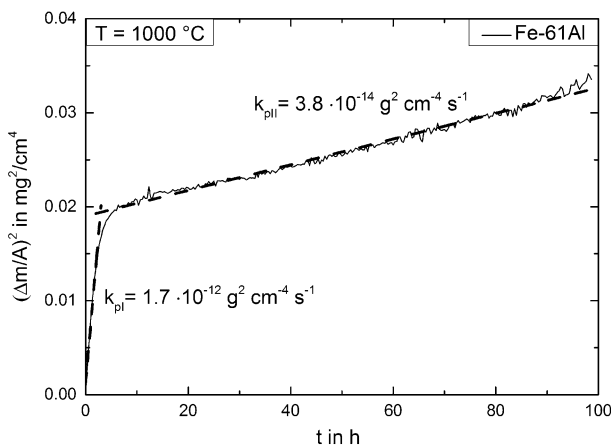


Fig. 5 Squared normalized mass gain vs. time plot for Fe–61Al at 1000 °C. The two determined k_p values were fitted as *dashed straight lines* to the respective parts of the oxidation curve

Table 2 Isothermal parabolic rate constants at 900 and 1000 °C

Alloy	k_p in $\text{g}^2 \text{cm}^{-4} \text{s}^{-1}$ at 900 °C	k_p in $\text{g}^2 \text{cm}^{-4} \text{s}^{-1}$ at 1000 °C
Fe–58Al	2.9×10^{-13}	$k_{p,I}$ 1.3×10^{-12}
		$k_{p,II}$ 4.4×10^{-14}
Fe–61Al	2.9×10^{-13}	$k_{p,I}$ 1.7×10^{-12}
		$k_{p,II}$ 3.8×10^{-14}
Fe–64Al	2.9×10^{-13}	$k_{p,I}$ 1.9×10^{-12}
		$k_{p,II}$ 1.1×10^{-13}

To identify the crystal structure of the grown alumina, GIXRD was exemplarily carried out on the eutectoid alloy after various hours of oxidation at 1000 °C. As shown in Fig. 6, mainly θ - Al_2O_3 with some amount of α - Al_2O_3 could be detected after 5 h of oxidation. With increasing oxidation time the intensity of α - Al_2O_3 peaks increases, whereas the intensity of θ - Al_2O_3 peaks decreases simultaneously. After 50 h nearly no θ - Al_2O_3 can be detected anymore and only α - Al_2O_3 prevails. This result clearly shows that within the first few hours θ - Al_2O_3 is formed, which obviously is transformed to α - Al_2O_3 during ongoing oxidation. Furthermore, it now

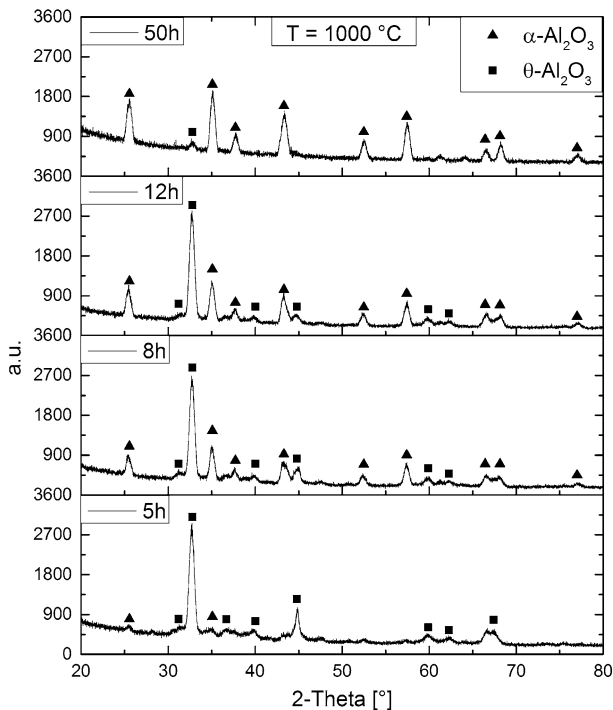


Fig. 6 GIXRD plots measured with a grazing incidence angle of 0.5° on the oxide scale of Fe-61Al subsequent to various exposure times at 1000 °C

seems conclusive that the measured $k_{p,I}$ values observed at the beginning of oxidation, which yield a fast mass gain (see Fig. 4a, b), can be attributed to the growth of θ - Al_2O_3 , whereas the $k_{p,II}$ values characterize the kinetics of α - Al_2O_3 formation during further oxidation. The significant bending in the oxidation curve after ~ 5 h at 1000 °C is, thus, caused by a phase transformation from θ - to α - Al_2O_3 . The oxidation rate of α - Al_2O_3 is, as shown in Fig. 5 and Table 2, significantly lower than that of θ - Al_2O_3 . This particular behavior is equal for all alloys and caused by the fact that diffusion of oxygen through the α - Al_2O_3 oxide scale is more inhibited as compared to θ - Al_2O_3 [16, 18, 19].

The fact that θ - Al_2O_3 transforms to α - Al_2O_3 , which are both known to be rate controlling oxides, is also the reason why the parabolic rate constants were determined by squared mass gain vs. time plots as recommended in [18, 19] (Fig. 5).

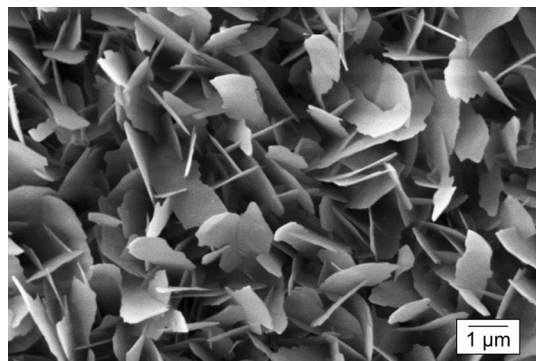
Oxide Scale

The oxide scale of the Fe–61Al after 99 h at 900 °C shows a whisker like morphology (see Fig. 7), which is typical for the appearance of metastable θ - Al_2O_3 [2, 5, 12, 13, 21].

Even though the oxidation kinetics changes at 1000 °C, the oxide scale (Fig. 8) exhibited also the whisker like structure of θ - Al_2O_3 as shown before in Fig. 7. The reason for this inherited morphology is that the main initial mass gain is caused by the growth of θ - Al_2O_3 . Even after the transformation into α - Al_2O_3 at larger exposure times the morphology is preserved, as the additional mass gain is comparatively low. Since this was also observed by Hindam and Smeltzer on B2-ordered NiAl, it can be assumed that the same mechanism takes place here [22]. The GIXRD data clearly support this: θ - Al_2O_3 transforms into α - Al_2O_3 . Furthermore, in some areas the whiskers seem to be coarsened and have formed concave cells (see Fig. 8). Those concave cells are comparable to those observed on NiAl by Rybicki and Smialek, who also assigned these flat circular regions to α - Al_2O_3 [19].

To investigate a possible selective oxidation and to proof if internal oxidation occurs, a cross-section of the microstructure was prepared. As shown in Fig. 9, a

Fig. 7 SEM-SE micrograph of the oxide scale on Fe–61Al after 99 h oxidation at 900 °C exhibiting θ - Al_2O_3 scale morphology



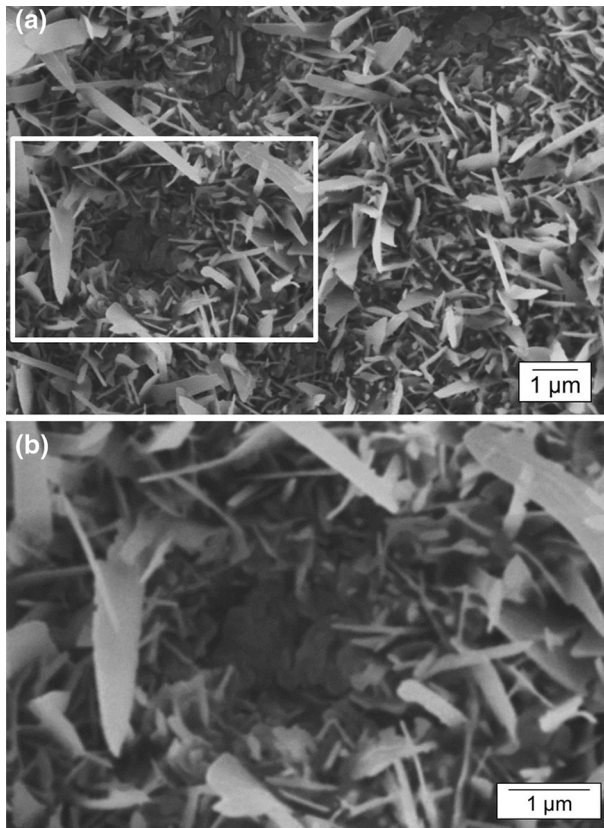


Fig. 8 SEM-SE micrograph of oxide scale on Fe–61Al after 99 h oxidation at 1000 °C **a** exhibiting the remaining θ -Al₂O₃ scale morphology and some flat circular areas of α -Al₂O₃, **b** higher magnification of highlighted area in **a** showing the flat circular areas of α -Al₂O₃

dense oxide scale has grown homogeneously on the alloy and selective oxidation of FeAl or FeAl₂ can be excluded. Therefore, it can be assumed that the oxidation behavior of both phases is comparable, and the differences in the crystallographic structure and aluminum content of the two phases have no significant influence on the oxidation behavior. Furthermore, no signs of internal oxidation along the phase boundaries are observed. Therefore, it can be inferred that in previous publications [13, 14] not the phase boundaries itself but rather the presence of reactive elements like Zr yield the nucleation sites for the observed internal oxidation.

Cyclic Oxidation

Since materials in technical applications are often exposed to thermal cycling, it is also important to study the oxidation behavior under cyclic conditions where spallation is promoted. Spallation leads to an abrupt mass loss and can be caused by several parameters such as (i) different thermal expansion coefficients of substrate

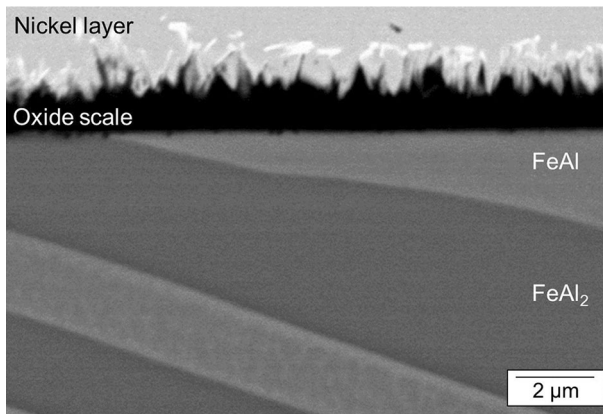


Fig. 9 SEM-BSE micrograph of a cross-section of the oxide scale on Fe–61Al after 99 h at 900 °C showing a dense grown Al_2O_3 scale on the two-phase microstructure covered by a Ni layer

and oxide scale, which result in interfacial stress during cooling and heating [23, 24] and for several alumina forming alloys (ii) poor adhesion between oxide scale and substrate due to segregation of sulfur at the interface metal/oxide [25–27].

To study the influence of thermal cycling on the oxidation behavior, cycling oxidation tests were carried out at 900 and 1000 °C. The reported mass change vs. time plot at 900 °C is shown in Fig. 10a. The resulting graphs essentially follow a square-root function and the kinetics can be described by the parabolic rate law (Eq. 1). Furthermore, no abrupt mass loss is observable, which leads to the assumption that no spallation occurs.

The determined parabolic rate constants are listed in Table 3 and are rather similar for all investigated alloys.

Oxidation tests under cyclic conditions at 1000 °C, however, show a mass loss of the alloys Fe–58Al and Fe–61Al (see Fig. 10b). Therefore, the parabolic rate law is not applicable and no rate constant could be determined. Even though the mass gain of the Fe–64Al alloy indicates almost a square root function (Fig. 10b), the investigation of the surface scale in the next section will demonstrate that massive spallation has occurred, and hence, a determination of a parabolic rate constant is also illegitimate.

Oxide Scale

For all investigated alloys the oxide scales after 550 h at 900 °C show the same whisker-like morphology and are basically similar to those under isothermal conditions (see Fig. 7). As has been already explained above, the whisker-like structure indicates the growth of $\theta\text{-Al}_2\text{O}_3$. It should be mentioned, that under cyclic conditions some small areas exist, where the oxide scale has spalled off (not shown here). However, since the k_p values are comparable to those under isothermal

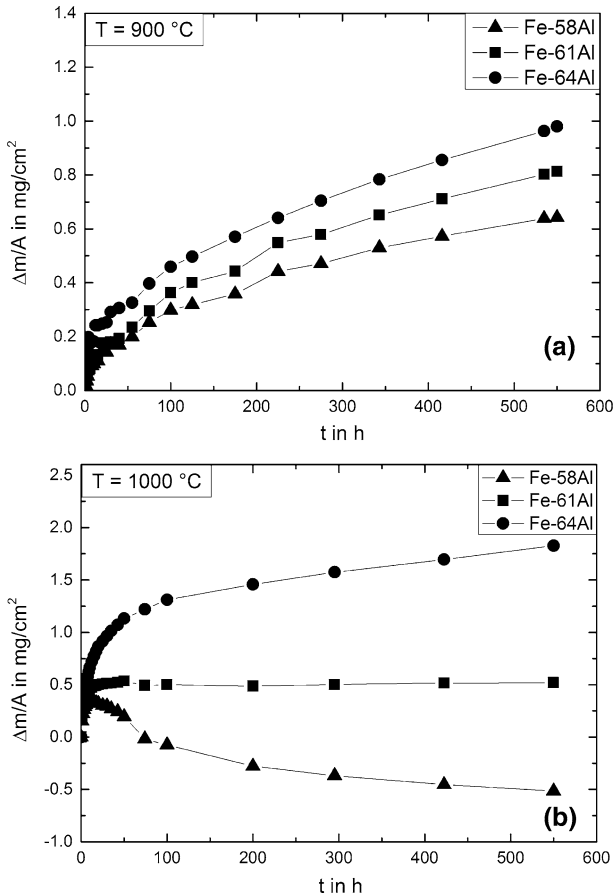


Fig. 10 Mass gain vs. time plot under cycling conditions of investigated alloys **a** at $900\text{ }^\circ\text{C}$, **b** at $1000\text{ }^\circ\text{C}$. Each data point represents a separate measurement after cooling from annealing temperature. The lines are added to guide the eye

Table 3 Parabolic rate constants under cycling conditions at $900\text{ }^\circ\text{C}$

Alloy	k_p in $\text{g}^2\text{ cm}^{-4}\text{ s}^{-1}$
Fe-58Al	2.4×10^{-13}
Fe-61Al	3.3×10^{-13}
Fe-64Al	4.6×10^{-13}

conditions, the influence of these “spalled off areas” is still considered to be negligible.

Although the mass gain vs. time plot of the Fe-64Al at $1000\text{ }^\circ\text{C}$ follows almost a square-root function (see Fig. 10b), a SEM-BSE image of the grown oxide scale proves that massive spallation has taken place (Fig. 11). Evidently, the bright areas

in the BSE contrast micrograph resemble the bare metal surface, which was also proven by EDX analysis (not shown here). The oxide scales on Fe–61Al and Fe–58Al after 550 h at 1000 °C under cycling condition are comparable to the oxide scale of the Fe–64Al and show also massive spallation. Since areas of spallation start to oxidize again, the continuous interplay between spallation and oxidation leads to a varying mass change, which is considerably different compared to isothermal tests at the same condition. Such a behavior under cyclic conditions at 1000 °C was already observed for NiAl [28]. The “spalled off areas” typically have diameters of 60–120 μm and are obviously responsible for the mass loss shown in Fig. 10. They also exhibit hollows (white arrows Fig. 11). The appearance of such hollows was first observed in oxidized NiAl [20, 22, 29]. Those are caused by outward diffusion of Al, where it is preferentially consumed during the formation of the oxide scale. The depletion of Al leads to a concurrent enrichment of Fe (or Ni in [18, 24, 29]) in the bulk material underneath the interface metal/oxide. As a consequence, an inward concentration gradient of Fe resulted. The material transport of Al and Fe leads to the formation of pores in the bulk material underneath the oxide scale. It is thus believed, that the observed hollow areas may be caused by this Kirkendall effect, in agreement with the observations by Yamauchi et al. [30].

These hollows obviously reduce the adhesion of the oxide scale. Further, spallation of the oxide scale may be promoted by stresses at the interface metal/oxide. In general, these stress are mainly caused by the mismatch of thermal expansion between oxide and metal during cool down [24] and by growth stresses occurring during oxidation [24, 31, 32]. However, Hou et al. have shown in intermetallic aluminides that S segregations can weaken the interface metal/oxide drastically [27]. Thereby, a S content above 1 ppm was found to be sufficient to promote spallation even in continuous oxidation trials [25, 27, 33]. In this case it was observed that the oxide scales exhibit a “wrinkled” morphology characteristic

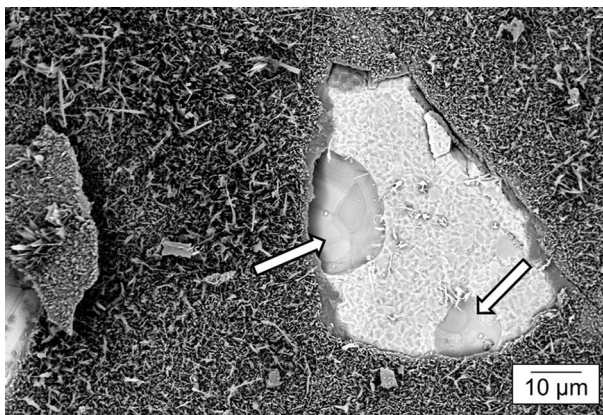


Fig. 11 SEM-BSE micrograph of oxide scale on Fe–64Al after 550 h at 1000 °C under cycling condition. The bright areas are bare metal where the oxide scale has spalled off. The arrows exemplarily mark some Kirkendall pores, which have formed underneath the oxide scale during oxidation

for S being segregated at the interface [27, 34]. Since in the present alloys no wrinkling behavior was observed for an S content of 5 wppm after 550 h under cyclic conditions at 1000 °C (Fig. 11), it may be concluded that S does not deteriorate oxide scale adherence.

Kinetics

Finally an attempt is made to comparatively assess the k_p values of Al-rich Fe–Al alloys investigated here with literature data on single phase B2-ordered FeAl alloys. The Arrhenius-plot in Fig. 12 shows the temperature dependence of the parabolic rate constant for growth of θ - and α -Al₂O₃ based on data of earlier isothermal oxidation studies on Fe–48Al [5]. The k_p values can be split into two regions, indicated by the two shaded areas, which symbolize either the growth rates of metastable θ -Al₂O₃ in a temperature range of 800–1000 °C or the ones of stable α -Al₂O₃ at even higher temperatures.

The determined k_p values under isothermal conditions for Fe–61Al and under cyclic condition for all investigated alloys at 900 °C clearly fall into the θ -Al₂O₃ region. The determined rate constants fit well with the ones for iron aluminides with aluminum contents in the range of 40–48 at.% [5]. This is reasonable, since Ryl'nikov et al. have already shown that at 900 °C the influence of an aluminum content in a range between 32 and 48 at.% (B2 phase-region) on the oxidation rate is negligible [35]. Since the k_p value at 900 °C for Fe–50Al [36] is slightly above the k_p values presented here, it may be concluded that the differences between the k_p values are caused by measurement inaccuracy and not due to deviations in the Al content.

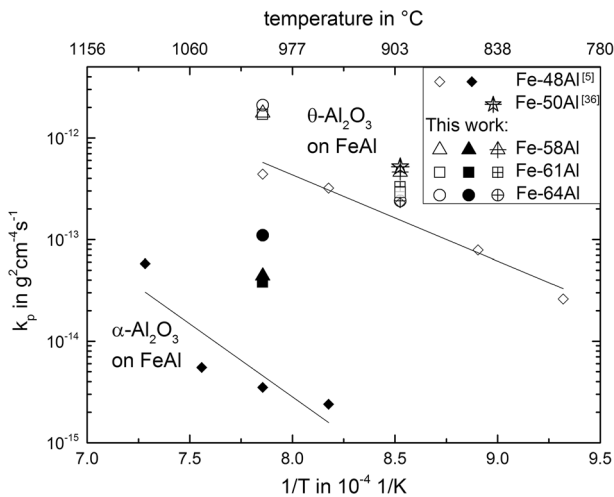


Fig. 12 Arrhenius plot for parabolic rate constants of Fe–48Al [5], Fe–50Al [36] and the determined k_p of the investigated alloys. The *full* and *open* symbols indicate the formation of α -Al₂O₃ and θ -Al₂O₃, respectively. The data points of the cyclic tests are marked by crosses

The $k_{p,I}$ and $k_{p,II}$ values at 1000 °C from isothermal oxidation tests are also plotted in Fig. 12. Here, it can be concluded that $k_{p,I}$ values evaluated during the first few hours of oxidation are clearly located in the region of θ -Al₂O₃ growth, whereas the $k_{p,II}$ values found for exposure times >5 h are substantially below the rate constants for θ -Al₂O₃ growth. Consequently, these $k_{p,II}$ constants may be attributed to the slower growing α -Al₂O₃ (as proved by XRD measurements).

Summary and Conclusions

The isothermal and cyclic oxidation behavior of Fe–Al alloys with Al contents of 58, 61 and 64 at.% were studied at 900 and 1000 °C in air. The morphologies, crystal structures and growth kinetics of the oxide scales were investigated. The most important conclusions are listed below:

- The determined parabolic rate constants at 900 °C under isothermal and cyclic conditions are comparable and spallation was found negligible.
- Under cyclic conditions massive spallation occurred in all investigated alloys at 1000 °C. No spallation was observed at isothermal test conditions.
- During the investigated time intervals of 99 and 550 h under isothermal and cyclic oxidation, respectively, at 900 °C θ -Al₂O₃ grew exclusively.
- At 1000 °C and isothermal test conditions, a change in oxidation kinetics occurs after 2–4 h. The nature of this change in oxidation kinetics could clearly be attributed to the transformation from θ -Al₂O₃ to α -Al₂O₃, which also coincides nicely with the determined parabolic rate constants. Since the period where the transformation took place was found to be similar for all alloys, it can be concluded that the oxidation behavior is independent of the volume fraction of the FeAl and FeAl₂ intermetallic compounds and of the aluminum content.
- Neither selective nor internal oxidation occurred in the alloys under the given test conditions.

Acknowledgements The authors gratefully acknowledge the German Research Foundation (DFG) within the project “Fein-lamellare Fe–Al in situ Kompositwerkstoffe”. Furthermore, we like to thank Prof. E.P. George and C.A. Carmichael from Oak Ridge National Laboratory for providing their instruments and assistance during arc melting of the alloys.

References

1. R. Prescott and M. J. Graham, *Oxidation of Metals* **38**, 73 (1992).
2. H. J. Grabke, *Intermetallics* **7**, 1153 (1999).
3. J. H. DeVan and P. F. Tortorelli, *Advanced Corrosion Protection* **35**, 1065 (1993).
4. C. Xu, W. Gao and H. Gong, *Intermetallics* **8**, 769 (2000).
5. I. Rommelskirchen, B. Eltester and H. J. Grabke, *Materials and Corrosion* **47**, 646 (1996).
6. P. Tomaszewicz and G. R. Wallwork, *Oxidation of Metals* **19**, 165 (1983).
7. F. Saegusa and L. Lee, *Corrosion* **22**, 168 (1966).
8. V. Kolarik, H. Fietzek, W. Engel, B. Eltester and H. J. Grabke, *Material Science Forum* **251–254**, 251 (1997).

9. W. E. Boggs, *Journal of Electrochemical Society* **118**, 906 (1971).
10. P. Kofstad, *High Temperature Corrosion*, (Elsevier, London, 1988).
11. W. Hagel, *Corrosion* **21**, 316 (1965).
12. J. L. Smialek, J. Doychak and D. J. Gaydosh, *Oxidation of Metals* **34**, 259 (1990).
13. D. Janda, H. Fietzek, M. Galetz and M. Heilmaier, *Intermetallics* **41**, 51 (2013).
14. A. Hotář, M. Palm, P. Kratochvíl, V. Vodičková and S. Daniš, *Corrosion Science* **63**, 71 (2012).
15. F. Stein and M. Palm, *International Journal of Materials Research* **98**, 580 (2007).
16. F. Stein, S. C. Vogel, M. Eumann and M. Palm, *Intermetallics* **18**, 150 (2010).
17. X. Li, M. Palm, A. Scherf, D. Janda, M. Heilmaier, and F. Stein, Proc. MRS Adv. Struct. Funct. Intermet.-Based Alloys Boston (2014).
18. B. Pieraggi, *Oxidation of Metals* **27**, 177 (1987).
19. G. C. Rybicki and J. L. Smialek, *Oxidation of Metals* **31**, 275 (1989).
20. H. J. Grabke, *Materials Science Forum* **251–254**, 149 (1997).
21. B. A. Pint, J. R. Martin and L. W. Hobbs, *Solid State Ionics* **78**, 99 (1995).
22. H. M. Hindam and W. W. Smeltzer, *Journal of the Electrochemical Society* **127**, 1630 (1980).
23. F. H. Stott, *Material Science Forum* **251–254**, 19 (1997).
24. V. K. Tolpygo and D. R. Clarke, *Oxidation of Metals* **49**, 187 (1998).
25. M. Stasik, F. Pettit, G. Meier, A. Ashary and J. Smialek, *Scripta Metallurgica Materialia* **31**, 1645 (1994).
26. J. G. Smeggil, A. W. Funkenbusch and N. S. Bornstein, *Metallurgical Transactions A* **17**, 923 (1986).
27. P. Y. Hou, A. P. Paulikas, B. W. Veal and J. L. Smialek, *Acta Materialia* **55**, 5601 (2007).
28. S. Yang, F. Wang and W. Wu, *Intermetallics* **9**, 741 (2001).
29. M. W. Brumm and H. J. Grabke, *Corrosion of Science* **33**, 1677 (1992).
30. A. Yamauchi, M. Tsunekane, K. Kurokawa, S. Hanada and K. Yoshimi, *Intermetallics* **18**, 412 (2010).
31. A. Huntz and M. Schutze, *Materials at High Temperature* **12**, 151 (1994).
32. V. K. Tolpygo, J. R. Dryden and D. R. Clarke, *Acta Materialia* **46**, 927 (1998).
33. J. Smialek, *JOM* **52**, 22 (2000).
34. Z.-G. Yang and P. Y. Hou, *Materials Science and Engineering A* **391**, 1 (2005).
35. B. S. Ryl'nikov, G. V. Arkhangel'skaya and L. V. Lyubetskaya, *Protection of Metals* **17**, 290 (1981).
36. Y. Kitajima, S. Hayashi, T. Nishimoto, T. Narita and S. Ukai, *Oxidation of Metals* **73**, 375 (2010).